

Tunable Enhancement of Raman Scattering in Graphene-Nanoparticle Hybrids

Kannan Balasubramanian,* Laura Zuccaro, and Klaus Kern

The realization of graphene-gold-nanoparticle (G-AuNP) hybrids is presented here through a versatile electrochemical approach, which allows the continuous tuning of the size and density of the particles obtainable on the graphene surface. Raman scattering from graphene, which is significantly enhanced in such hybrids, is systematically investigated as a function of the size and density of particles at the same location. In agreement with theory, it is shown that the Raman enhancement is tunable by varying predominantly the density of the nanoparticles. Furthermore, it is observed that the increase in Raman cross-section and the strength of Raman enhancement varies as a function of the frequency of the vibrational mode, which may be correlated with the plasmonic fingerprint of the deposited AuNPs. In addition to this electromagnetic enhancement, support is found for a chemical contribution through the occurrence of charge transfer from the AuNPs onto graphene. Finally, G-AuNP hybrids can be efficiently utilized as SERS substrates for the detection of specifically bound non-resonant molecules, whose vibrational modes can be unambiguously identified. With the possibility to tune the degree of Raman enhancement, this is a platform to design and engineer SERS substrates to optimize the detection of trace levels of analyte molecules.

1. Introduction

Hybrid nanostructures obtained by combining nanomaterials of different dimensions present unique possibilities that are not directly obtainable in their constituent structures. By judiciously combining the advantages of 2D and 0D nanostructures we obtain new properties and interesting characteristics that open avenues for novel applications as well as for fundamental research. Graphene is an ideal 2D material with just one layer of carbon atoms, with unique electrical and mechanical properties.^[1–3] Nanoparticles (NPs) due to their 0D character provide extraordinary optical properties such as the existence of localized surface plasmon resonances (LSPR) in the visible.^[4–7] By bringing together these two classes of systems it is expected that the optical properties of 0D nanostructures can

be efficiently merged with the electrical properties of graphene to realize new kinds of optoelectronic and electrooptic devices.^[8,9] One of the major effects of the presence of nanoparticles in the vicinity of 1D or 2D nanostructures is the enhancement in Raman scattering attributed to LSPR of the particles^[10–12] and/or the presence of near-fields due to coupled resonances at ensembles of nanoparticles (hot spots).^[11,13,14]

Until now, however most of these hybrids have mainly been realized by direct deposition of nanoparticles (including gold) on graphene or by placing graphene on a surface with gold nanostructures.^[10,12,14–18] One major limitation of such methods^[12,14,16] is the difficulty in measuring the Raman enhancement at the same location as a function of variation in particle size and/or density. Moreover in almost all these cases,^[10,12,14–18] the gold nanostructures have been positioned by some form of lithography, which poses

some limitations on the size and spacing of the attainable particles. Electrodeposition of metal by reducing a metal salt in solution is a facile method to obtain nanoparticles on graphene.^[19–23] We have first demonstrated the possibility to obtain Pd nanoparticles on reduced graphene oxide, where the electrical characteristics of the obtained hybrids were in focus.^[19] Electrochemical modification (ECM) of graphene with gold and silver nanoparticles has also been investigated in other contexts,^[20–23] but the interesting optical properties arising from such hybrids have been seldom investigated. The first major advantage in using electrodeposited nanoparticles is that the size and density of nanoparticles can be varied at the same location and the effect of this variation on the Raman enhancement in graphene studied in a systematic manner. This avoids ambiguities arising from the variable nature of Raman enhancement that is typically observed due to the inhomogeneous distribution of particle size and density and the random nature of occurrence of hot spots.^[13,24] Secondly, unlike other reported graphene-nanoparticle hybrids we do not require the need for extensive lithographic patterning or cleanroom processing. Apart from these aspects, the capability to tune the particle size and density provides a new handle for modulating the plasmonic response^[25–30] of the realized graphene-nanoparticle (G-AuNP) hybrids.

Here, we present a systematic investigation of the evolution of Raman enhancement by observing the same graphene region

Dr. K. Balasubramanian, Dr. L. Zuccaro, Prof. K. Kern
Max Planck Institute for Solid State Research
Heisenbergstrasse 1, D-70569 Stuttgart, Germany
E-mail: b.kannan@fkf.mpg.de

Prof. K. Kern
Institut de Physique de la Matière Condensée
Ecole Polytechnique Fédérale de Lausanne
CH-1015, Lausanne, Switzerland



DOI: 10.1002/adfm.201401796

as a function of increasing particle size and density. We observe a clear correlation between the strength of Raman enhancement and the nanoparticle size and density and identify key parameters that play a crucial role in tuning this enhancement. We present a detailed analysis of the influence of nanoparticles on the various vibrational modes of graphene and obtain information about the mechanisms of Raman enhancement. Finally, we demonstrate that such hybrid structures can be used as substrates for surface-enhanced Raman spectroscopy (SERS) to sensitively detect the presence of specifically bound analyte molecules.

2. Results and Discussion

Figure 1 presents important details of the fabrication of graphene-nanoparticle hybrids and the observed Raman spectra. Chemical vapor deposition (CVD)-grown graphene is transferred onto silicon substrates using polystyrene or poly (methylmethacrylate) as a support.^[31] The copper foil underneath graphene is etched in a solution of HCl with added H₂O₂. Figure 1a shows an AFM image of a typical graphene region obtained using this method. After measuring reference Raman spectra at selected locations, gold nanoparticles are deposited

on the surface using electrochemical modification (ECM). For this purpose a gold salt in an aqueous electrolyte is reduced at an appropriate potential.^[32] We have preferred to use gold in place of another metal such as silver because the electrodeposition of gold does not require any additional growth control agent (such as poly(vinylpyrrolidone), needed for silver electrodeposition),^[32] which may interfere with the Raman signals. The details of the electrodeposition procedure can be found in the Experimental Section and Supporting Information (Figure S1). Figure 1b presents the same graphene area after electrodeposition showing clearly the formation of nanoparticles at a low density with heights in the range of 20–60 nm (see Figure S2 for line profile analysis). The formation of particles (rather than a continuous film) is attributed to a spatial variation in reactivity arising due to various factors including defects.^[33,34] This leads to local nucleation sites resulting in the formation of small metallic islands.^[35] Figures 1c,d show the Stokes and anti-Stokes Raman spectra before and after ECM at the same spot with the same set of instrumental parameters. It is apparent that the intensities of the Raman bands have significantly increased after ECM. Most notably anti-Stokes D and G peaks can be clearly observed only after the attachment of nanoparticles.

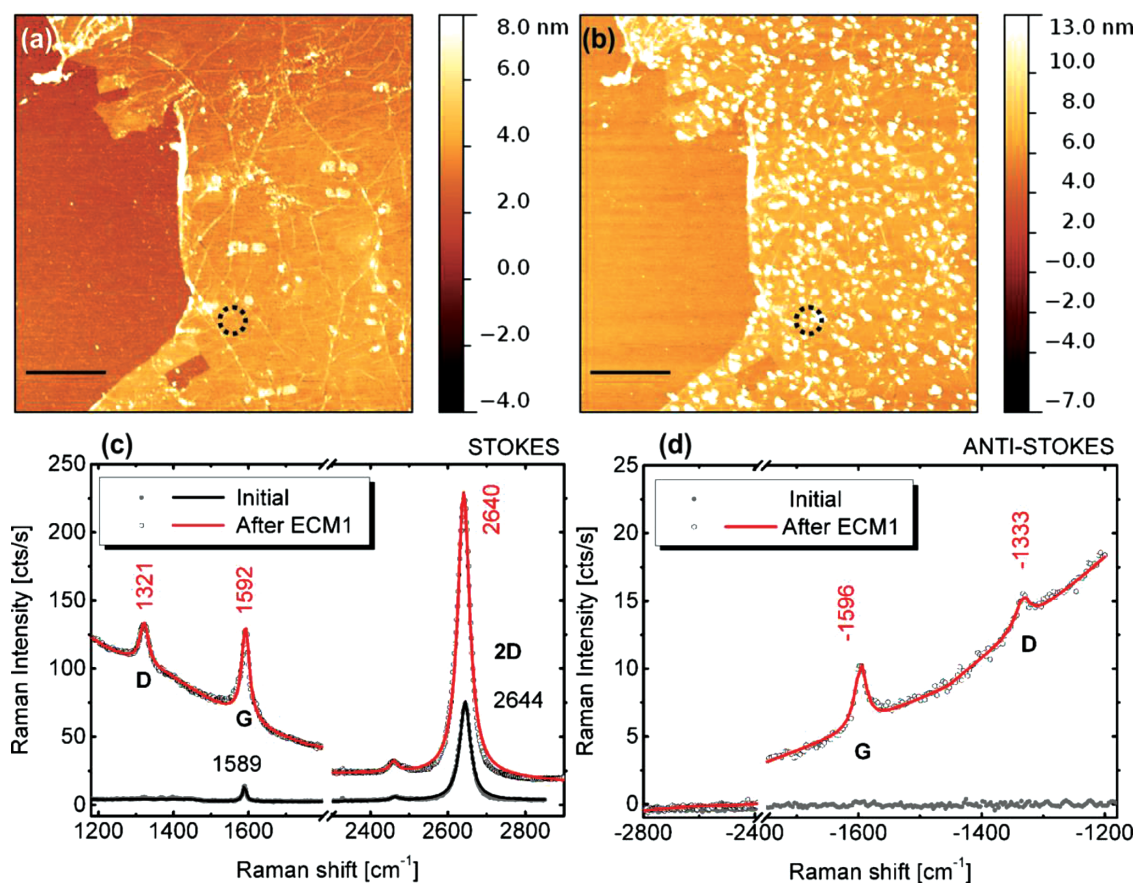


Figure 1. Raman enhancement in G-AuNP hybrids. AFM images of transferred CVD-graphene a) before and b) after deposition of gold nanoparticles. Scale bar is 2 μm . The electrochemical modification (ECM) is performed at -0.7V vs open circuit in a solution of 0.2 mM KAuCl_4 in aqueous 0.09 M LiClO_4 . c) Stokes and d) anti-Stokes Raman spectra before and after the deposition of nanoparticles at the location marked by the circle in (a,b). The data points are fitted with Lorentzians and a baseline to identify the peak positions of the various graphene modes. The errors in the peak positions are less than 1 cm^{-1} . λ_{ex} : 633 nm , power: 4 mW , integration time: $6 \times 20\text{ s}$. See also Figure S2 in Supporting Information for line profile analysis.

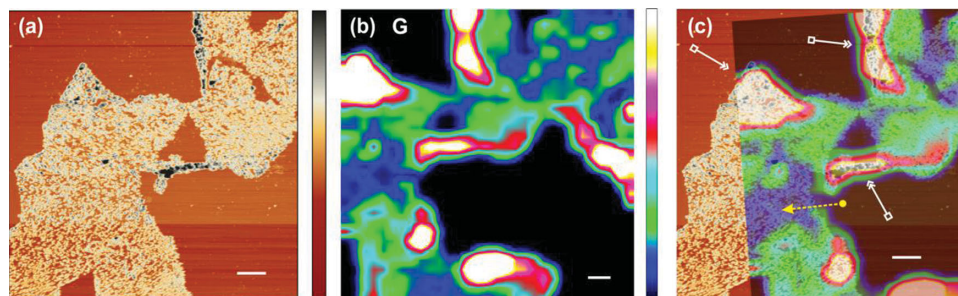


Figure 2. Spatial variation of Raman enhancement in G-AuNP hybrids. a) AFM image of a selected area, with big particles highlighted by a black pseudo color map (b) Raman map of the same region (integrated intensity around the G peak : 1560–1610 cm^{-1}). (c) Overlay of AFM image and Raman map to identify the spatial origin of Raman enhancement. The yellow dashed arrows indicate areas of low particle density, while the white solid lines with double arrows highlight regions of tall particles. The X-/Y-scale bars are 2 μm in all images. The Z-scale bars are: a) 110 nm, e) 250 (avg. counts/s). λ_{ex} : 633 nm, power: 4 mW, integration time per point: 2×3 s.

The spectra in Figure 1 present a number of interesting aspects, which require further investigation. First, in addition to the enhancement of the Raman peaks, the signals show a clear background, which is virtually zero on bare graphene. This background may be attributed to the fluorescence of nanoparticles similar to observations made on carbon nanotubes decorated with gold nanoparticles.^[36] The fluorescence arises due to recombination of photoexcited carriers at the band edges of the L- and X-points (in reciprocal space) in gold nanostructures and is characteristic of nanoparticles with diameters less than 150 nm.^[37,38] The occurrence of this fluorescence and the ensuing Raman enhancement are related to plasmonic resonances of the deposited nanoparticles.^[11,38–40] Secondly, the position of the 2D and G peaks (obtained by fitting Lorentzians) shift slightly after decoration with nanoparticles. Furthermore, the intensity ratio of the D- to G-peaks has increased and is now close to one. Both these are indicative of the presence of some kind of a chemical interaction between the nanoparticles and graphene.^[41] Finally an important question concerns the effect of the size, shape and density of the nanoparticles on the extent of Raman enhancement. In the following, we will address these aspects one after the other.

The spatial variation in Raman enhancement was investigated by obtaining Raman maps, whereby entire spectra were acquired as a function of position. We focus in the main text on the behavior of the G-peak. **Figure 2a,b** presents an AFM image and a map of the integrated G-peak intensity after decoration with nanoparticles. **Figure 2c** presents an overlay of the AFM image and Raman map in order to identify the spatial origin of the Raman signal. As marked with the yellow dashed arrow in **Figure 2c**, it is apparent that the Raman signal is weakest at locations of low particle density. On the other hand, the intensity is significantly higher at locations (white solid lines with double arrows), where there are bigger nanoparticles (highlighted with a black pseudo color scale in the AFM image). A qualitatively similar behavior is also observed for the 2D-peak maps as presented for another location in the Supporting Information (**Figure S3**). From these observations we conclude that there is a correlation between the observed Raman enhancement and both the size as well as the density of the obtained nanoparticles.

The challenge here is to attain the ability to tune the distribution of nanoparticles and thereby aim for a control over

the strength of Raman enhancement. ECM presents a unique possibility to achieve this control by modulating the size and density of nanoparticles using an appropriate choice of electrochemical parameters.^[42] Towards this goal, we have obtained Raman maps of the same location after 6 consecutive steps of electrodeposition. The electrochemical parameters are chosen in such a way that in the first three steps, the sizes of the nanoparticles on graphene predominantly increase, with little variation in density. In the latter three steps a higher overpotential is used to increase also the density of the nanoparticles. The conditions for obtaining this variation are discussed further in the Supporting Information (**Figure S4**).

Figure 3 collects AFM and Raman G-peak maps of the same location at the initial stage and after the first 3 ECM steps. From the AFM images of **Figures 3(a-d)**, it can be seen that the particles increase in height at a rough average of 10 nm every ECM step (histograms of particle heights are shown in **Figure S5**). The regions where the size increase is predominant are marked in these AFM images. **Figures 3e–h** present Raman G-peak maps of a slightly larger area encompassing the region of the AFM image. The area where the AFM image was acquired is marked as a square in these Raman maps. It is apparent that after every ECM step the G-peak intensity is found to increase. This is however not perfectly homogeneous in the entire mapped area. This may be attributed to a variation in particle sizes, and a broad distribution of inter-particle spacing obtained on the graphene surface.^[43–45] The Raman maps in **Figures 3e–h** plot the directly measured G-band intensity and hence also include the background fluorescence that was discussed in **Figure 1**. **Figures 3i–l** present Raman maps of the same area by excluding this fluorescence background using a baseline subtraction of the spectrum at every point. It is striking that in these images an enhancement is seen only after the first ECM step and not anymore in the subsequent two steps. (Note that in the upper left corner of the Raman images the intensity is higher because of a large fold/multilayer present there.) From these observations we conclude that increasing particle height mainly leads to an increase in the fluorescence background, which coherently enhances the absolute intensity of the observed Raman peaks. The background-subtracted Raman intensity appears to depend on the interfacial surface area between the AuNPs and graphene, which does not change much after the first ECM.

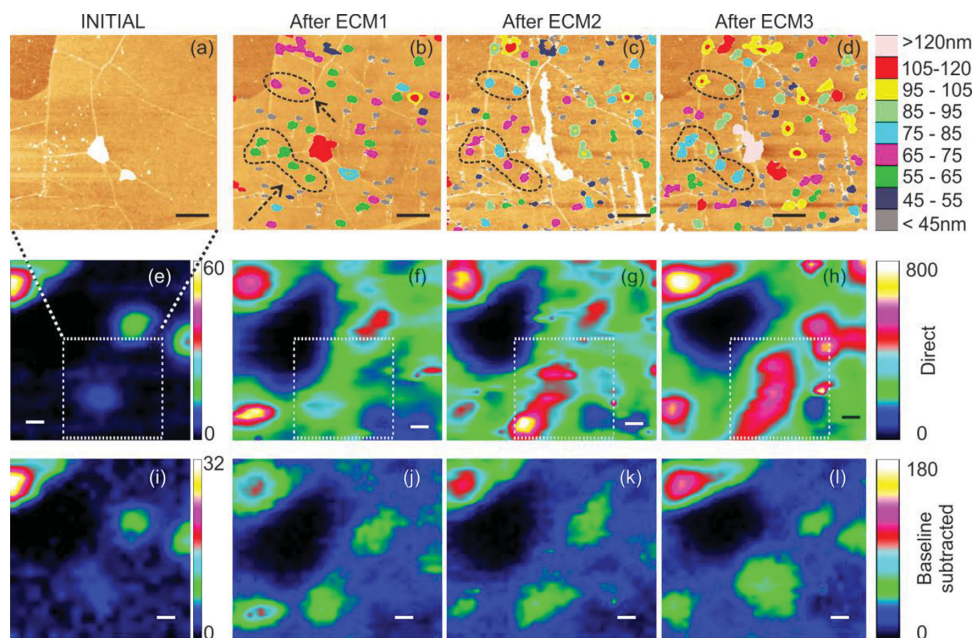


Figure 3. Raman enhancement with increasing particle size. The first row shows AFM images of the same area a) before and b–d) after 3 consecutive electrochemical modification (ECM) steps. The top left corner in the AFM images shows a hole in the graphene sheet. The same pseudo color scale is used for all the images. The grains in the image are first identified and subsequently color-coded according to their heights. It is apparent that in the marked areas, the heights of the particles increase with every ECM step without the introduction of new particles. e–h) Raman maps of the G-peak intensity (integrated from 1560–1610 cm^{-1}). i–l) The same maps after a baseline subtraction at every point. The area shown here is slightly larger encompassing the region of the AFM images. The area in the Raman maps where the AFM images were taken is identified with a square. As mentioned in the text, the spectra with AuNPs have a broad fluorescence background. The images in the second row include this background, while those in the third row do not. It is clear that the Raman intensities in the second row increase from (e) to (h), while those in the third row from (j) to (l) do not. Please note that the intensity is high in the top left corner of the Raman maps since the graphene sheet is folded (multilayer) there. X-/Y-scale bar for all images is 1 μm . λ_{ex} : 633 nm, power: 4 mW, Integration time per point: 2×3 s. Please note that the Z-scale for (e) is different from the other maps. The long vertical white stain in (c) is most likely due to a particle that is dragged by the AFM tip.

Figure 4 presents a similar set of images as in Figure 3 but after the ECM steps 3, 4 and 6 in the same graphene region. From the AFM images in Figures 4a,b it can be seen that the parameters were chosen in such a way that there is a local increase in particle density marked by the ellipse, while from Figure 4c it can be seen that the density increase occurs everywhere. Figure 4d–f presents direct G-peak maps, while Figure 4g–i presents the baseline-subtracted G-peak maps. It is clear that unlike in Figure 3, we have an enhancement in the Raman intensity in both the cases. By taking these two datasets together it can be concluded that the density of particles plays a more dominant role in achieving a significant Raman enhancement. It appears that smaller particles at a high density will be the most efficient route to obtain maximal Raman enhancement with a minimal fluorescence background.

The rather qualitative picture presented above based on Figure 3, 4 agrees well with a theoretical model that has been proposed for Raman enhancement in graphene-nanoparticle hybrids.^[12] According to this model, the Raman enhancement due to a standalone nanoparticle is given by

$$\frac{\Delta I_{\text{SERS}}}{I_0} \approx \frac{3}{28} \sigma Q^2(\omega) Q^2(\omega_s) \left(\frac{a}{h}\right)^{10} \quad (1)$$

where ΔI_{SERS} is the increase in Raman intensity with respect to the original intensity I_0 , σ is the relative cross-sectional

area of the nanoparticle, $Q(\omega)$ is the plasmonic enhancement in absorption due to the nanoparticle obtainable from Mie scattering theory with ω_s representing the Raman Stokes frequency, a the radius of nanoparticle and h the distance of the particle centre from the surface of graphene. The increase in Raman scattering with increase in particle size (as in Figure 3) can be mainly attributed to the plasmonic absorption profile $Q(\omega)$ of the nanoparticles. The shapes of the particles vary a lot over the graphene surface, although it can be expected that a majority of them are hemispherical. Simulations of the extinction cross-section have shown that the plasmonic resonances for gold particles in the size range of 60–120 nm lie around the laser excitation wavelength of 633 nm (see Supporting Information, Figure S6).^[36,46] This is also confirmed by obtaining absorption spectra of the G-AuNP hybrids as a function of particle size and density (see Figure S7). Moreover the absorption spectrum becomes broader as the particle size increases. As a result, the $Q(\omega)$ term contributes to a continuous increase in Raman enhancement as the particle grows. On the other hand the a/h ratio decreases with increasing height of the particle, explaining the comparatively weaker effect of size increase on the Raman enhancement. With increasing density (as shown in Figure 4) however, the effective average cross-section (σ) of the particles under the laser spot increases. The newly created particles additionally contribute with their plasmonic absorption profile ($Q(\omega)$) and a good a/h ratio due to the small initial

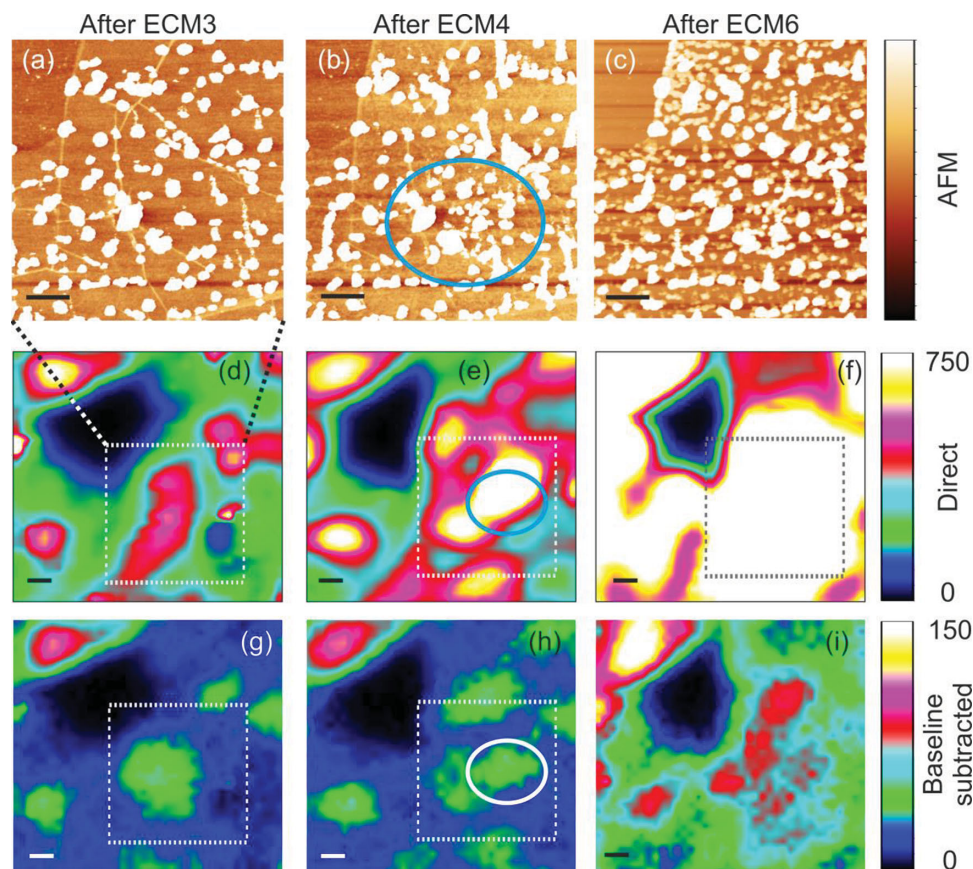


Figure 4. Raman enhancement with particle density. The first row shows AFM images of the same area as in Figure 3 after the a) third, b) fourth, and c) sixth ECM steps. The top left corner in the AFM images shows a hole in the graphene sheet. The density increases from (a) to (b) mainly in an area marked with the ellipse in (b). From (b) to (c) there is an overall increase in density. d–f) Raman maps of the G-peak intensity (integrated from 1560–1610 cm^{-1}). g–i) The same maps after a baseline subtraction at every point. As mentioned in the text, the spectra with AuNPs have a broad fluorescence background. The images in the second row include this background, while those in the third row do not. The areas common in the Raman map and AFM images are identified with the ellipses. It is clear that the Raman intensities increase in both the second and third rows as we go from left to right (in contrast to Figure 3). Please note that the intensity is high in the top left corner of the Raman maps since the graphene sheet is folded there. X-/Y-scale bar for all images is 1 μm . λ_{ex} : 633 nm, power: 4 mW, Integration time per point: 2×3 s. The Z-scale bar for AFM images are a) 20 nm, b) 25 nm, and c) 65 nm.

height. These factors consistently explain the stronger Raman enhancement when the nanoparticle density increases.

The model discussed above however does not include contributions from coupled resonances that may occur due to the presence of hot spots, for example, due to particle dimers.^[13,14,47,48] The spatial variation in Raman intensity may be partly attributed to the presence of such hot spots. However, we do not see a clear correlation between features in the AFM images and the peaks of intensity in the Raman maps, most likely due to the comparatively larger spot size of the laser. At the first instance, one may expect a very large enhancement at such hot spots,^[10,11,13,48] which are most likely present in our samples due to many different configurations of particle arrangements. However, in the 4 different series of experiments that we have carried out, the maximum intensity (for all the three modes – G, D and 2D) in a region (such as in Figures 2,3 or 4) differs from the minimum intensity at most by a factor of 7. This is nevertheless in agreement with experimental studies on the systematic effect of variable dimer spacing on Raman enhancement, where it has been shown that

the Raman enhancement at a dimer hot spot is at most an order of magnitude larger than at isolated nanoparticles.^[44,45] Due to this aspect we attribute the randomly occurring maxima in the Raman intensity predominantly to the occurrence of hot spots. Furthermore, there is also recent evidence that even single molecules can be detected using SERS at isolated nanoparticles.^[49]

In order to have a quantitative idea of the extent of enhancement we have specifically followed the enhancement at many different spots (7 different spots for the sample in Figures 3 and 4) after every ECM step. A representative set of spectra is presented in Figure 5. The background shift and the apparent increase in the Raman intensities are well reproduced for the D- and G-peaks both in the Stokes and anti-Stokes side of the spectra in Figures 5a,b. The 2D peak intensities shown in Figure 5c increase overall, however the increase is not consistent in every step. We have observed the same trend in the other locations. Figure 5d shows the enhancement factor for the various Raman modes as a function of ECM steps (based on the direct intensity without baseline subtraction). It is clear that the degree of enhancement is not the same for all the

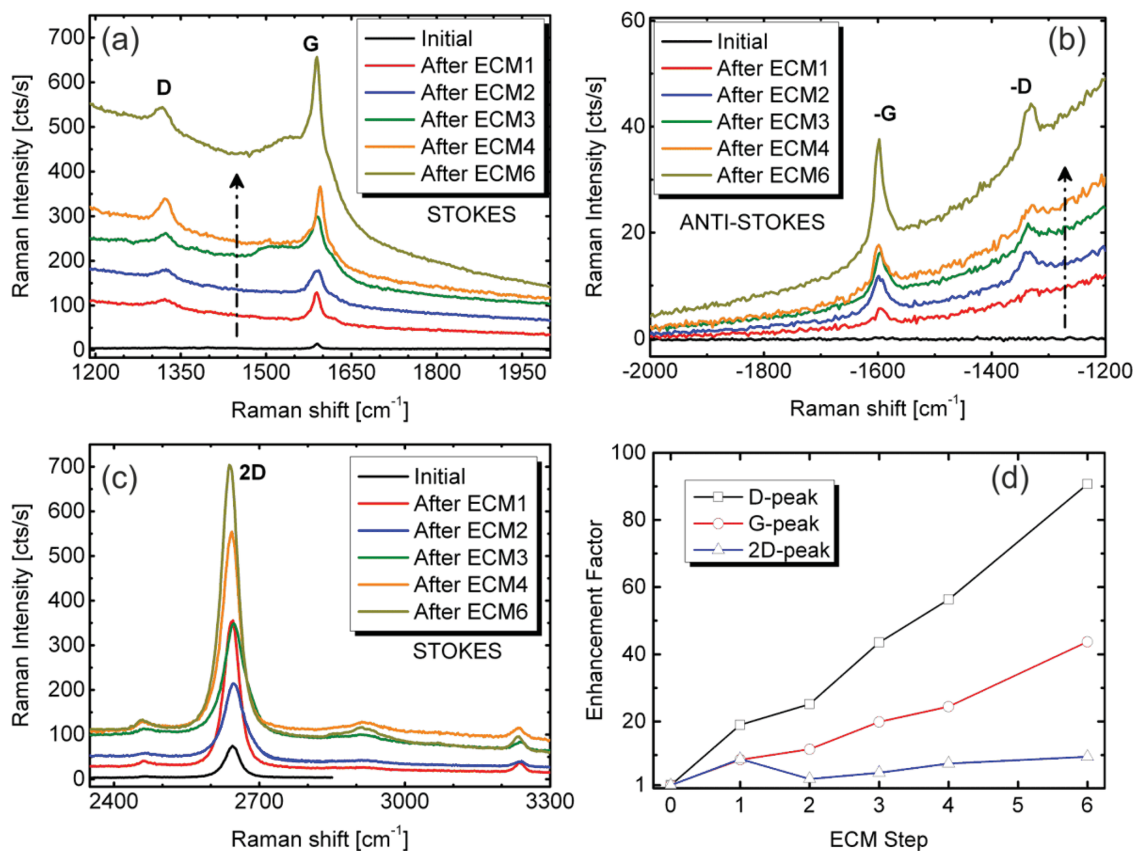


Figure 5. Tunable Raman enhancement in G-AuNP hybrids. Raman spectra at the same location before and after the various electrochemical modification (ECM) steps: a) Stokes D- and G-peak region, b) anti-Stokes D- and G-peak regions, c) 2D-peak region. The intensities of the Raman modes of graphene increase with every consecutive ECM step. d) Raw enhancement factor calculated as the ratio of the intensity after every ECM step to the initial intensity. λ_{ex} : 633 nm, power: 4 mW, Integration time per point: 6 × 20 s.

graphene modes and becomes weaker as the frequency of the vibrational mode increases. This can be directly understood when one considers again Equation (1), where the frequency dependence enters through the $Q(\omega_s)$ term, which incorporates the induced polarizability of the nanoparticle due to the excited dipole at the Raman Stokes frequency ω_s .^[12] In fact, such a frequency-dependent Raman enhancement (correlated with the plasmonic profile, see also Figures S6 and S7) has been clearly observed for the detection of the vibrational modes of rhodamine 123 on silver colloids.^[50] For the spectra in Figure 5, we see a maximum enhancement of around 100 after the step 6 of ECM. Similar factors were obtained for the other locations, with the highest observed enhancement factor of around 240. It is worth mentioning that this is a true enhancement factor obtained directly since we have an unambiguous measurement of the Raman signal with and without nanoparticles. Such direct information is unavailable in all other reported experiments, where a derived enhancement factor is computed by making a range of assumptions including the number of molecules and the nature of the excited near field at the particles.^[24,47,51–54]

Further support for the Raman shift-dependent enhancement is gathered by analyzing the intensity ratios of the anti-Stokes to Stokes (AS/S) graphene vibrational bands. The AS/S intensity ratio is generally given by

$$\rho(\omega_R) = \left(\frac{\sigma_{AS}}{\sigma_S} \right)_R \left(\frac{\omega_{\text{ex}} + \omega_R}{\omega_{\text{ex}} - \omega_R} \right)^4 \exp(-\hbar\omega_R / k_B T_G) \quad (2)$$

where ω_R and ω_{ex} are the frequencies of the Raman mode and laser excitation respectively; σ_S and σ_{AS} are the Stokes and anti-Stokes Raman cross-sections, which are also a function of ω_R and T_G is an effective temperature determining the occupation number of phonons in graphene under laser illumination.^[55–57] The ratio (σ_{AS}/σ_S) is an asymmetry factor, which differs from 1 if resonance effects are present that modulate the Raman cross-section at the AS and S frequencies.^[24] In order to estimate the phonon temperature T_G we show a scatter plot of the AS/S intensity ratios of D-peak against those of the G-peak in Figure 6a. These data points are obtained from the Stokes and anti-Stokes map of the same region as in Figure 4 (after ECM4). A clear correlation can be seen between the two AS/S ratios. Using a linear fit of the data we can extract a slope, from which we estimate T_G to be of the order of 900 K.^[58] This temperature is however just a measure of the apparent increase in the phonon population and corresponds to a real temperature increase to less than 350 K.^[59] Interestingly, this value is similar for the data obtained after ECM3, ECM4 and ECM6. Figures 6b,c show histograms of the G-peak (ρ_G) AS/S ratios after ECM4 and ECM6 respectively. It is clear that the AS/S ratios have increased after the final ECM. From Equation 2 it

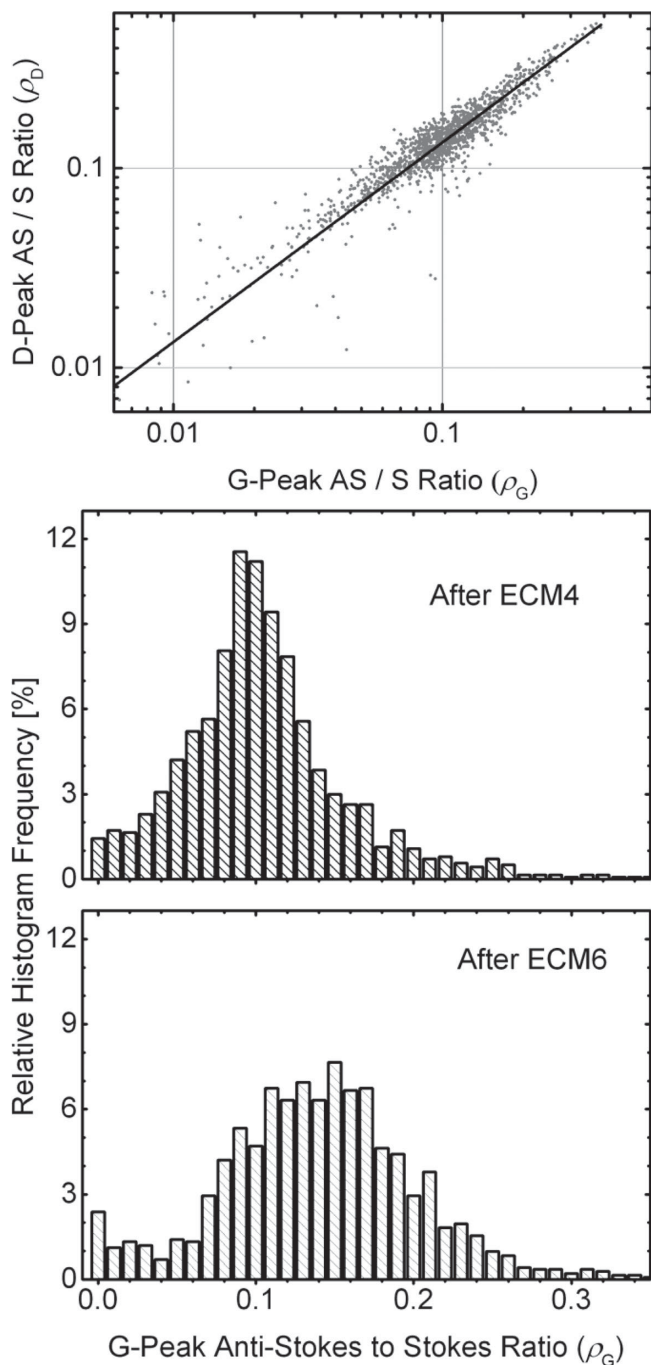


Figure 6. Anti-Stokes-to-Stokes Ratio in G-AuNP hybrids. a) Scatter plot of D-peak anti-Stokes to Stokes ratio against that for the G-peak after ECM4, in order to estimate the phonon temperature T_G . The values are obtained from the Raman maps of the same region as shown in Figure 3, 4. The solid line shows a linear fit to the data plotted in a log-log-scale. b,c) Histograms of the AS-S-ratios after ECM4 (b) and after ECM6 (c) for the G-peak as obtained from the Raman maps. The histogram and the scatter plot are obtained from about 1400 spectra.

can be seen that the most likely way this can happen is by an increase in the asymmetry factor (σ_{AS}/σ_S). We attribute this relative increase in anti-Stokes Raman cross-section to the availability of plasmonic resonances.^[24,25] This can be justified by

observing that the anti-Stokes G mode (-1596 cm^{-1} or 575 nm) has a higher energy than the energy level spacing at the X-point ($\approx 617 \text{ nm}$), while the energy of the Stokes G-mode ($+1596 \text{ cm}^{-1}$ or 704 nm) is less than the energy spacing at both the L- and X- points.^[37,38] We observe a similar increase in the AS/S ratio also for the D-peak as shown in the Supporting Information (Figure S8). In this manner, we have demonstrated for the first time that the deposited nanoparticles clearly bring in a vibrational mode-dependent increase in Raman cross-section, which can be traced back to the plasmonic nature of the nanoparticles.

Now we turn towards the nature of chemical interaction between the nanoparticles and graphene. For this purpose, we analyze the position of the G- and 2D-peaks in the Raman maps obtained after the various ECM steps as shown in Figure 7a,b.

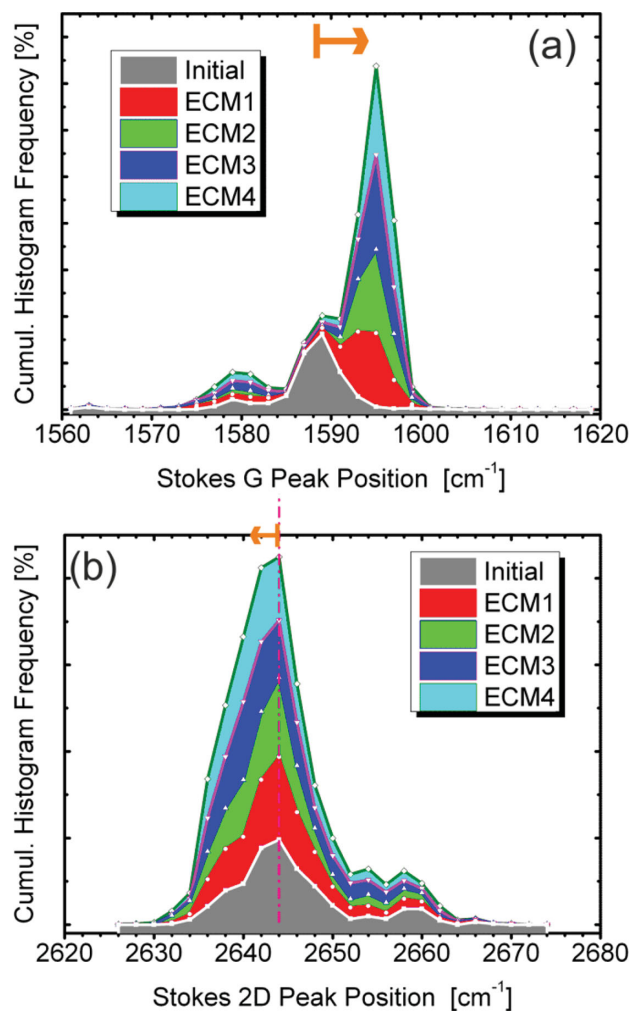


Figure 7. Charge transfer from AuNPs on to graphene. Histograms of a) G-peak and b) 2D-peak positions from the Raman maps of Figure 3, 4. The peak positions are identified from the Raman spectrum at every pixel. The graphs present a histogram of these peak positions before and after every ECM step. The G-peak position is found to shift to higher wavenumbers, while the 2D peak shifts slightly to lower wavenumbers (indicated by the orange arrows). The G-peak shift is strong only after the two initial ECM steps. The histograms are presented as stacked area plots, with the Y-axis showing the cumulative frequency of occurrence. Every Raman map contains around 1400 spectra.

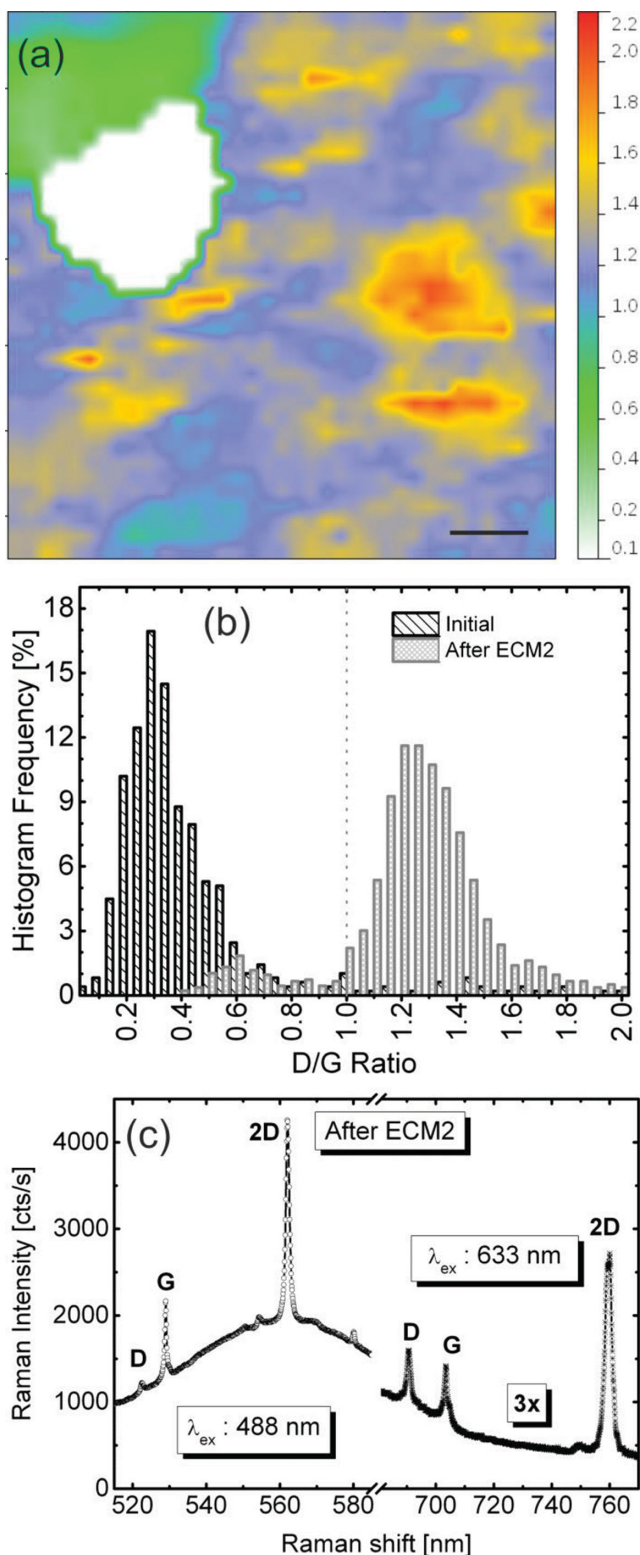


Figure 8. D-to-G ratio (I_D/I_G) in G-AuNP hybrids. a) Map of the ratio of Raman D-peak to Raman G-peak intensity after ECM step 2. Scale bar is 2 μm . b) Histogram of the ratio values from the Raman I_D/I_G maps obtained initially and after ECM2. It is clear that I_D/I_G values are much higher after attachment of nanoparticles. c) Raman spectra obtained at the same spot after ECM2 using two different laser excitation wavelengths

The G-peak shifts to higher wavenumbers by around 6 cm^{-1} after the first ECM step, after which it remains more or less constant with only a slight shift with every subsequent ECM step. On the other hand the 2D-peak shifts slightly to lower wavenumbers continuously with every subsequent ECM step. Both these shifts are consistent with electron transfer from the nanoparticles on to graphene.^[60] The extent of charge transfer is however not so strong most likely due to the similar work functions of gold and graphene.

Figure 8a presents a map of the D-to-G peak intensity ratio (I_D/I_G) of the same region as in Figure 3, 4) exemplarily after ECM step 2. In order to compare the magnitude of the ratios, Figure 8b presents histograms of I_D/I_G before and after ECM2. It is apparent that the D/G ratio shows a significant increase after attachment of nanoparticles. However it does not increase much during the subsequent ECM steps. In order to evaluate if I_D/I_G may still be correlated with increased disorder, we have measured the Raman spectra at certain locations using two different laser excitation (633 nm and 488 nm). As shown in Figure 8c, it is clear that I_D/I_G is high for the 633 nm excitation, while it is much lower for the 488 nm excitation. It is known that the disorder-related I_D/I_G values increase with increasing laser wavelength.^[61] Based on the relations presented for quantifying disorder in graphene,^[61,62] we estimate a defect spacing (L_D) in the range of 24–36 nm (low defect density regime), after correcting by a factor of 2 for the frequency-dependent enhancement (estimated from Figure 5d). We fix L_D in the low defect-density regime since the FWHM of the 2D-peak is around 40 cm^{-1} and the position of the G-peak does not shift as a function of the laser wavelength.^[61,63] It is worth mentioning that in many other positions, we do not observe such a strong I_D/I_G , and correspondingly the defect density is typically lower than this value. These aspects lead us to conclude that the nanoparticles are non-covalently bound on the surface. However they are intimately attached in such a way to induce charge transfer on to underlying graphene. Most likely this chemical interaction adds constructively to the observed Raman enhancement.^[64,65] A remote possibility is the selective enhancement of D-peak intensity due to charge transfer analogous to wavelength dependent charge transfer enhancement observed on silver clusters.^[19] Future experiments by varying laser excitation wavelength may shed light on this aspect.

The availability of a strong resonant enhancement in G-AuNP hybrids motivates their use as substrates for the detection of analyte molecules via surface enhanced Raman spectroscopy (SERS). Typically gold or silver colloids with LSPR in the visible range are deployed as SERS substrates. Such colloids or nanoparticles immobilized on different surfaces including graphene have allowed the detection of trace amounts of analytes.^[10,11,13] Here we show that G-AuNP hybrids can be utilized to detect specifically bound thiolated molecules. Towards this goal, we incubated the G-AuNPs in a dilute (10 μM) solution of 2-mercapto-pyridine (2-mpy) in ethanol for 2 h followed by copious rinsing

of comparable power (2.7 mW). The I_D/I_G value is lower than 1 with the 488 nm excitation, while it is higher than 1 with the 633 nm excitation. Moreover, the fluorescence background from the particles is more prominent in the spectrum acquired with 488 nm excitation. The 633 nm spectra are magnified by a factor of 3.

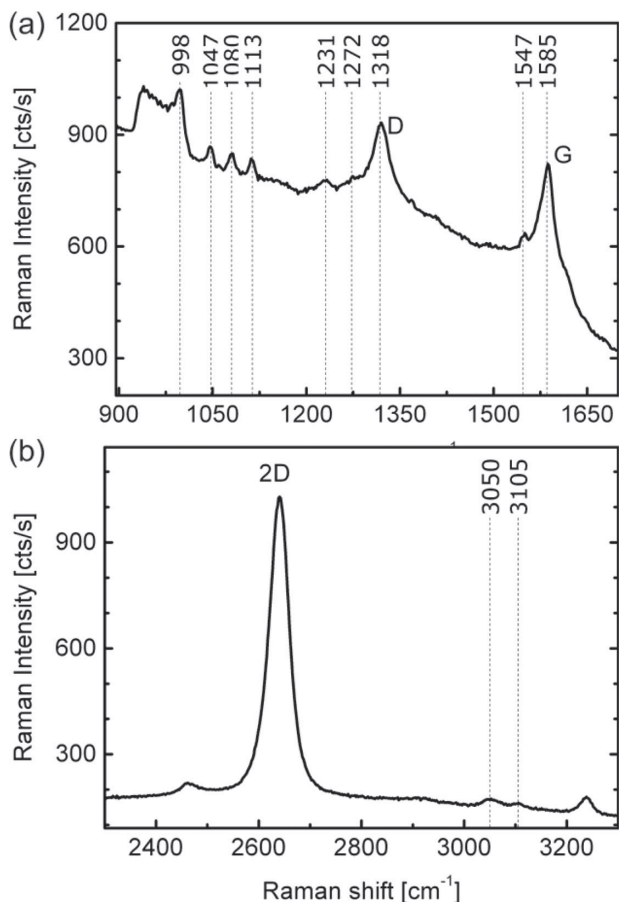


Figure 9. SERS detection of non-resonant molecules. Raman spectra from 2-mercaptopyridine molecules specifically bound on G-AuNP hybrids: a) graphene D-/G-peak region, b) graphene 2D-peak region. The binding was carried out by incubating the G-AuNP hybrid in a 10 μm solution of 2-mercaptopyridine in ethanol for 2 h. The peak positions are indicative values with a spread of roughly $\pm 3 \text{ cm}^{-1}$. In addition to the graphene peaks (identified as D, G, and 2D) the peaks originating from 2-mercaptopyridine are identified by their corresponding values of Raman shifts (see Table 1). λ_{ex} : 633 nm, power: 4 mW, Integration time per point: $6 \times 20 \text{ s}$.

in ethanol. This protocol that is typically used in the realization of self-assembled monolayers (SAMs) ensures that we have at most a single layer of 2-mpy molecules on the nanoparticles in the ideal situation.^[66,67] After drying the sample, Raman spectra were acquired, a representative example of which is shown in Figure 9. The peak-positions shown in the Figure are extracted by visual examination (see also Figure S9 for more spectra). In addition to the graphene-related peaks we observe new peaks, which can be associated with the vibrational modes of the immobilized 2-mpy molecules. By comparison with literature values,^[68–70] we can assign the peaks to specific modes of 2-mpy unambiguously (see Table 1). It is worth mentioning that however, we did not see any of the 2-mpy bands on the anti-Stokes side of the spectrum. Moreover, we did not see the peaks on bare graphene after incubation with 2-mpy consistent with the expectation that there is no specific interaction between graphene and 2-mpy. In order to ensure that the observed peaks are indeed due to a SERS effect from the nanoparticles, we have

Table 1. Assignment of the various peaks in the spectra of Figure 9 to vibrational modes of 2-mercaptopyridine.

Raman shift [cm^{-1}] ($\pm 3 \text{ cm}^{-1}$)	Vibrational mode	Symmetry	Wilson mode
998	ring breathing	A_g	1 or 1a
1047	C–H wag	A'	18a
1080	C–H wag	A_g	18b
1113	Ring breathing/C–S stretch	A', B_u	12 or 12a
1231	N–H	A_g	
1272	C=C / C–N	A', A_g	14b
1318	Graphene D		
1547	C=C stretch	A'	8b
1585	Graphene G		
2640	Graphene 2D		
3050	C–H stretch		
3105	C–H stretch		

repeated the measurements on the AuNPs alone after removing graphene by an oxygen plasma etch, where we can also observe the vibrational modes of 2-mpy (see Figure S10).

3. Conclusion

In summary, we have demonstrated a versatile route for tuning the strength of Raman enhancement through the realization of electrodeposited nanoparticles on a graphene surface. Through astute control over the particle size and density at the same location of interest, we have shown that—in agreement with theory—the enhancement in Raman scattering is tightly related to the cross-sectional area at the nanoparticle/graphene interface. The mechanism of enhancement could be traced back to both an electromagnetic nature arising due to plasmonic resonances and a chemical contribution manifesting in the form of charge transfer on to graphene. Moreover, we have followed for the first time the evolution of the SERS enhancement factors at the same location as the particle size and density increase. This enabled us to show that SERS enhancement in graphene is dependent on the frequency of the vibrational mode. Finally, we presented a proof-of-principle showing the capability of G-AuNP hybrids to detect just a monolayer of analyte molecules self-assembled on their surface. The versatility of our approach allows the possibility of attaching nanoparticles of other metals such as Pd, Pt or Ag and thereby obtain another degree of tunability that is unparalleled with currently available metal-nanoparticle hybrids.

4. Experimental Section

Graphene-on-copper was procured from Graphene Supermarket Inc. First, poly(methylmethacrylate) or polystyrene is coated on the obtained copper foil either by spin coating or drop casting. After a short baking for 2 min at 80 $^{\circ}\text{C}$, the copper is etched in a solution of HCl/ H_2O_2 . The etching is complete in less than 10 min. After rinsing the

polymer/graphene slab in dilute HCl and deionized water, the flake is fished out using a Si/SiO₂ chip with prepatterned Ti/Pt electrode lines. The electrode lines serve as leads to contact graphene to perform the electrodeposition. Raman spectra are obtained from a LabRam HR equipped with an 800 mm monochromator, a 600 l/mm grating, a HeNe laser with an excitation wavelength of 632.8 nm and a detection pinhole of 100 or 140 micrometers. The power was maintained at 4 mW for almost all of the acquisitions. Only the data in Figure 8c were obtained using a NT-MDT NTEGRA system, where the laser excitation was switchable between 488 nm and 632.8 nm at a fairly constant power of 2.7 mW. This system was equipped with a 520 mm monochromator and a 600 l/mm grating. Confocal Raman images were obtained by scanning the sample stage below the diffraction-limited laser spot and recording Stokes/anti-Stokes spectra at every scan point. The data were processed using LabSpec 5 and Origin. Peak-fitting was done using Origin assuming Lorentzian lineshapes for all of the important bands. Acquisition times for images ranged from 2 × 2 s to 2 × 5 s, while for point spectra they were fixed at 6 accumulations of 20 s each. AFM images and Raman maps were processed by Gwyddion. The electrochemical modification was performed in a 3-electrode cell with graphene acting as a working electrode, a 0.5 mm Pt wire working as counter and a Ag/AgCl electrode acting as a reference. The final concentrations of the metal salt and the background electrolyte for all the depositions were 0.2 mM KAuCl₄ and 0.09 M LiClO₄ in water. The solutions were always freshly prepared right before the deposition.

Supporting Information

Supporting Information is available from the Wiley Online Library or from the author. Supporting information presents details of electrochemical modification of graphene, line profiles of AFM images in Figure 1, 2D Raman maps of graphene-AuNP hybrids, AFM images after modification with AuNPs, histograms of particle distributions, simulated extinction spectra of gold nanoparticles, measured extinction spectra of G-AuNP hybrids, histograms of anti-Stokes to Stokes D-peak intensity ratios, more examples of the SERS spectra of 2-mpy, SERS spectra of 2-mpy on AuNPs alone (after etching graphene) and a calibration spectrum of HOPG.

Acknowledgements

The authors thank Mathieu Le Tacon, Jürgen Smet, Matthias Hepting, and Armin Schulz for access to, help with and discussion about the Raman measurements, as well as Stephan Schmid and Yvonne Link for metal electrode deposition.

Received: June 3, 2014

Revised: June 26, 2014

Published online: August 19, 2014

- [1] A. K. Geim, A. K. S. Novoselov, *Nat. Mater.* **2007**, *6*, 183–191.
- [2] A. K. Geim, *Science* **2009**, *324*, 1530–1534.
- [3] K. S. Novoselov, V. I. Falko, L. Colombo, P. R. Gellert, M. G. Schwab, K. Kim, *Nature* **2012**, *490*, 192–200.
- [4] M. Faraday, *Phil. Trans. R. Soc. Lond.* **1857**, *147*, 145–181.
- [5] U. Kreibitz, M. Vollmer, *Optical Properties of Metal Clusters*, Springer, Berlin-Heidelberg **1995**.
- [6] H. Horvath, *J. Quant. Spectr. Rad. Transf.* **2009**, *110*, 787–799.
- [7] S. A. Maier, *Plasmonics: Fundamentals and Applications*, Springer Berlin-Heidelberg **2007**.
- [8] P. H. Avouris, *IEEE J. Sel. Top. Quant. Elec.* **2014**, *20*, 6000112.

- [9] F. Bonaccorso, Z. Sun, T. Hasan, A. C. Ferrari, *Nat. Photonics* **2010**, *4*, 611–622.
- [10] W. Xu, X. Ling, J. Xiao, M. S. Dresselhaus, J. Kong, H. Xu, Z. Liu, J. Zhang, *Proc. Nat. Acad. Sci. U.S.A.* **2012**, *109*, 9281–9286.
- [11] W. Xu, N. Mao, J. Zhang, *Small* **2013**, *9*, 1206–1224.
- [12] F. Schedin, E. Lidorikis, A. Lombardo, V. G. Kravets, A. K. Geim, A. N. Grigorenko, K. S. Novoselov, A. C. Ferrari, *ACS Nano* **2010**, *4*, 5617–5626.
- [13] K. Kneipp, H. Kneipp, I. Itzkan, R. R. Dasari, M. S. Feld, *Chem. Rev.* **1999**, *99*, 2957–2975.
- [14] S. Heeg, R. Fernandez-Garcia, A. Oikonomou, F. Schedin, R. Narula, S. A. Maier, A. Vijayaraghavan, S. Reich, *Nano Lett.* **2013**, *13*, 301–308.
- [15] P. Wang, W. Zhang, O. Liang, M. Pantoja, J. Katzer, T. Schroeder, Y.-H. Xie, *ACS Nano* **2012**, *6*, 6244–6249.
- [16] Q. Hao, B. Wang, J. A. Bossard, B. Kiraly, Y. Zeng, I.-K. Chiang, L. Jensen, D. H. Werner, T. J. Huang, *J. Phys. Chem. C* **2012**, *116*, 7249–7254.
- [17] C. Yi, T.-H. Kim, W. Jiao, Y. Yang, A. Lazarides, K. Hingerl, G. Bruno, A. Brown, M. Losurdo, *Small* **2012**, *8*, 2721–2730.
- [18] M. Losurdo, C. Yi, A. Suvorova, S. Rubanov, T.-H. Kim, M. M. Giangregorio, W. Jiao, I. Bergmaier, G. Bruno, A. S. Brown, *ACS Nano* **2014**, *8*, 3031–3041.
- [19] M. Sun, S. Liu, M. Chen, M. Xu, *J. Raman Spectrosc.* **2008**, *40*, 137–143.
- [20] D. J. Lomax, I. A. Kinloch, R. A. W. Dryfe, *12th IEEE Conference on Nanotechnology* **2012**, 1–4, DOI: 10.1109/NANO.2012.6322218.
- [21] J. C. Claussen, A. Kumar, D. B. Jaroch, M. H. Khawaja, A. B. Hibbard, D. M. Porterfield, T. S. Fisher, *Adv. Func. Mater.* **2012**, *22*, 3399–3405.
- [22] S. Wu, Z. Yin, Q. He, G. Lu, Q. Yan, H. Zhang, *J. Phys. Chem. C* **2011**, *115*, 15973–15979.
- [23] W. Zhao, X. Zhou, J. Chen, X. Lu, *J. Cluster Sci.* **2013**, *24*, 739–749.
- [24] R. C. Maher, L. F. Cohen, P. Etchegoin, H. J. N. Hartigan, R. J. C. Brown, M. J. T. Milton, *J. Chem. Phys.* **2004**, *120*, 11746–11753.
- [25] J. B. Jackson, N. J. Halas, *Proc. Natl. Acad. Sci. U.S.A.* **2004**, *101*, 17930–17935.
- [26] M. Kahraman, P. Daggumati, O. Kurtulus, E. Seker, S. Wachsmann-Hogiu, *Sci. Rep.* **2013**, *3*, 3396_1–9.
- [27] A. Wei, B. Kim, B. Sadtler, S. L. Tripp, *ChemPhysChem* **2001**, *12*, 743–745.
- [28] R. Alvarez-Puebla, B. Cui, J.-P. Bravo-Vasquez, T. Veres, H. Fenniri, *J. Phys. Chem. C* **2007**, *111*, 6720–6723.
- [29] W. Lee, S. Y. Lee, R. M. Briber, O. Rabin, *Adv. Funct. Mater.* **2011**, *21*, 3424–3429.
- [30] X. Lang, J. Li, X. Luo, Y. Zhang, Y. Yin, T. Qiu, *ChemPhysChem* **2014**, *15*, 337–343.
- [31] J. Song, F.-Y. Kam, R.-Q. Png, W.-L. Seah, J.-M. Zhuo, J.-M. G. K. Lim, P. K. H. Ho, L.-L. Chua, *Nat. Nanotechnol.* **2013**, *8*, 356–362.
- [32] K. Balasubramanian, M. Burghard, *J. Mater. Chem.* **2008**, *18*, 3071–3083.
- [33] A. G. Guell, N. Ebejer, M. E. Snowden, J. V. Macpherson, P. R. Unwin, *J. Am. Chem. Soc.* **2012**, *134*, 7258–7261.
- [34] G. L. Paulus, Q. H. Wang, M. S. Strano, *Acc. Chem. Res.* **2013**, *46*, 160–170.
- [35] R. S. Sundaram, C. Gomez-Navarro, K. Balasubramanian, M. Burghard, K. Kern, *Adv. Mater.* **2008**, *20*, 3050.
- [36] M. Scolari, A. Mews, F. Nan, A. Myalitsin, T. Assmus, K. Balasubramanian, M. Burghard, K. Kern, *J. Phys. Chem. C* **2008**, *112*, 391–396.
- [37] S. Eustis, M. El-Sayed, *J. Phys. Chem. B* **2005**, *109*, 16350–16356.
- [38] M. R. Beversluis, A. Bouhelier, L. Novotny, *Phys. Rev. B* **2003**, *68*, 115433–1:10.

- [39] F. Tam, G. P. Goodrich, B. R. Johnson, N. J. Halas, *Nano Lett.* **2007**, *7*, 496–501.
- [40] C. L. Haynes, R. P. van Duyne, *J. Phys. Chem. B* **2003**, *107*, 7426–7433.
- [41] A. C. Ferrari, *Sol. Stat. Commun.* **2007**, *143*, 47–57.
- [42] P. V. Dudin, P. R. Unwin, J. V. Macpherson, *J. Phys. Chem. C* **2010**, *114*, 13241–13248.
- [43] G. C. Schatz, R. P. van Duyne, *Handbook of Vibrational Spectroscopy*, (Eds: J. M. Chalmers, P. R. Griffiths), John Wiley, Chichester **2002**.
- [44] M. K. Hossain, G. R. Willmott, P. G. Etchegoin, R. J. Blaikie, J. L. Tallon, *Nanoscale* **2013**, *5*, 8945–8950.
- [45] K. D. Alexander, K. Skinner, S. Zhang, H. Wei, R. Lopez, *Nano Lett.* **2010**, *10*, 4488–4493.
- [46] P. K. Jain, K. S. Lee, I. H. El-Sayed, M. A. El-Sayed, *J. Phys. Chem. B* **2006**, *110*, 7238–7248.
- [47] C. E. Talley, J. B. Jackson, C. Oubre, N. K. Grady, C. W. Hollars, S. M. Lane, T. R. Huser, P. Nordlander, N. J. Halas, *Nano Lett.* **2008**, *5*, 1569–1574.
- [48] T. Assmus, K. Balasubramanian, M. Burghard, K. Kern, M. Scolari, F. Nan, A. Myalitsin, *Appl. Phys. Lett.* **2007**, *90*, 173109–1:3.
- [49] A. B. Zrimsek, A.-I. Henry, R. P. van Duyne, *J. Phys. Chem. Lett.* **2013**, *4*, 3206–3210.
- [50] T. Itoh, K. Yoshida, V. Biju, Y. Kikkawa, M. Ishikawa, Y. Ozaki, *Phys. Rev. B* **2007**, *76*, 085405.
- [51] E. C. Le Ru, E. Blackie, M. Meyer, P. G. Etchegoin, *J. Phys. Chem. C* **2007**, *111*, 13794–13803.
- [52] J. Kneipp, H. Kneipp, K. Kneipp, *Chem. Soc. Rev.* **2008**, *37*, 1052–1060.
- [53] P. G. Etchegoin, E. C. Le Ru, *Phys. Chem. Chem. Phys.* **2008**, *10*, 6079–6089.
- [54] E. Hao, G. C. Schatz, *J. Chem. Phys.* **2004**, *120*, 357–366.
- [55] K. Kneipp, H. Kneipp, I. Itzkan, R. R. Dasari, M. S. Feld, *J. Phys.: Cond. Mater.* **2002**, *14*, R597–R624.
- [56] H. Xu, J. Aizpurua, M. Kaell, P. Apell, *Phys. Rev. E* **2000**, *62*, 4318–4324.
- [57] R. C. Maher, L. F. Cohen, J. C. Gallop, E. C. Le Ru, P. G. Etchegoin, *J. Phys. Chem. B* **2006**, *110*, 6797–6803.
- [58] The use of this slope avoids the need for any specific calibration of the AS/S ratio (ρ) using standardized samples, since these effects must be similar at so close wavenumbers (between graphene D- and G-peaks).
- [59] D. H. Chae, B. Krauss, K. von Klitzing, J. H. Smet, *Nano Lett.* **2010**, *10*, 466–471.
- [60] A. Das, S. Pisana, B. Chakraborty, S. Piscanec, S. K. Saha, U. V. Waghmare, K. S. Novoselov, H. R. Krishnamurthy, A. K. Geim, A. C. Ferrari, A. K. Sood, *Nat. Nanotechnol.* **2008**, *3*, 201–215.
- [61] L. G. Cancado, A. Jorio, E. H. Martins Ferreira, F. Stavale, C. A. Achete, R. B. Capaz, M. V. O. Moutinho, A. Lombardo, T. S. Kulmala, A. C. Ferrari, *Nano Lett.* **2011**, *11*, 3190–3196.
- [62] M. M. Lucchese, F. Stavale, E. H. Martins Ferreira, C. Vilani, M. V. O. Moutinho, R. B. Capaz, C. A. Achete, A. Jorio, *Carbon* **2010**, *48*, 1592–1597.
- [63] We use the FWHM of 2D peak and not the D- or G-peak since the 2D peak is going to be least affected by the plasmonic resonances.
- [64] X. Jiang, A. Campion, *Chem. Phys. Lett.* **1987**, *140*, 95–100.
- [65] L. Zhao, L. Jensen, G. C. Schatz, *J. Am. Chem. Soc.* **2006**, *128*, 2911–2919.
- [66] L. Sun, C. X. Yu, J. Irudayaraj, *Anal. Chem.* **2007**, *79*, 3981
- [67] J. Baldwin, N. Schuhler, I. S. Butler, M. P. Andrews, *Langmuir* **1996**, *12*, 6389.
- [68] J. A. Baldwin, B. Vlckova, M. P. Andrews, I. S. Butler, *Langmuir* **1997**, *13*, 3744–3751.
- [69] N. Hassan, R. Holze, *Russ. J. Electrochem.* **2012**, *48*, 401–411.
- [70] N. M. S. Sirimuthu, C. D. Syme, J. M. Cooper, *Chem. Commun.* **2011**, *47*, 5099–4101.